analytical chemistry

pubs.acs.org/ac Article

Photocatalytic Fuel Cell-Assisted Molecularly Imprinted Self-Powered Sensor: A Flexible and Sensitive Tool for Detecting Aflatoxin B1

Yunxia Jin, Yang Luan, Zhen Wu,* Wei Wen, Xiuhua Zhang, and Shengfu Wang*

Cite This: *Anal. Chem.* 2021, 93, 13204−13211 Read Online

ACCESS | Metrics & More | Article Recommendations | Supporting Information

ABSTRACT: The self-powered electrochemical sensor has gained big achievements in energy and devices, but it is challenging in analytical application owing to its low energy conversion efficiency and limited selectivity caused by the plentiful interference in actual samples. Herein, a new self-powered biosensor was constructed by the integration of a photocatalytic fuel cell (PFC) with a molecular imprinting polymer (MIP) to achieve sensitive and specific detection of aflatoxin B1 (AFB_1). Compared with other fuel cells, the PFC owns the advantages of low cost, high energy, good stability, and friendly environment by using light as the excitation source. $MoS_2-Ti_3C_2T_x$ MXene (MoS_2-MX) served as the photoanode material for the first time by forming a heterojunction structure, which can enhance the photocurrent by about 3-fold and greatly improve the photoelectric conversion efficiency. Aiming at the poor selectivity of the self-powered sensor, the MIP was introduced to achieve the specific capture and separation of targets without sample pretreatment. Using the MIP and PFC as recognition and signal conversion elements, respectively, the proposed self-powered biosensor showed a wide dynamic range of 0.01−1000 ng/mL with a detection limit of 0.73 pg/mL, which opened opportunities to design more novel self-powered biosensors and promoted its application in food safety and environmental monitoring.

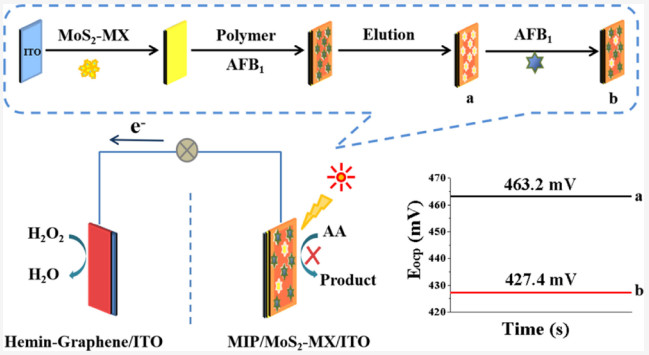

The self-powered electrochemical sensor (SPES) was first proposed by Willner et al.[1] in 2001 and has become a hot spot of research because of its simple operation, low cost, fast response, and the ability to be integrated with other technologies. A suitable battery system is constructed, and the sensor can realize analytical detection based on the output signal change of the battery caused by the interaction between targets and electrodes. Different from traditional three-electrode systems, this kind of SPES provides energy for detection through the spontaneous electrochemical reaction of the anode and cathode, without external power supply or voltage biasing, which is expected to realize unpowered and on-site detection.[2] As the energy conversion element of SPES, various fuel cells have been developed,[3] including microbial fuel cells,[4,5] enzymatic biofuel cells,[6,7] photocatalytic fuel cells (PFCs),[8] and so on. Among them, PFCs can directly convert light energy into electrochemical energy, owning the advantages of strong energy, good stability, and friendly environment by using light as the excitation source. PFC assisted self-powered sensors have received much attention and been applied in antibiotics,[9] pollutants,[10] and biomarker detection.[11] However, this sensor is difficult to satisfy the need of timely measurement of low-abundant targets ascribed to the limited photoelectric conversion efficiency. The development of multifunctional nanomaterials and electrode modification technologies brings new opportunities and breakthroughs for designing more novel and sensitive self-powered sensors.

MXene is a new 2D transition metal carbide/nitride/carbonitride, which was discovered and extensively studied in 2011.[12] The easy biofunctionalization of its surface makes MXene a promising alternative to graphene as a photocatalytic material.[13] The general formula for MXene is $M_{n+1}X_nT_x$ (n = 1−3), where M is a transition mental (such as Ti, Mo, Ta, or Cr), X is carbon or nitrogen, and T_x stands for surface functional groups (such as −OH, −O, −F, or −Cl).[14] Due to its abundant surface group, good electrochemical conductivity, and unique photocatalytic properties, MXene is widely used to improve the photocatalytic efficiency of semiconductors. Importantly, MXene has been reported to be a good carrier acceptor and rich in surface active groups,[13] opening up a new

Received: May 17, 2021
Published: September 16, 2021

https://doi.org/10.1021/acs.analchem.1c02074
Anal. Chem. 2021, 93, 13204−13211

Scheme 1. Illustration of the PFC-Assisted Self-Powered Biosensor for AFB_1 Detection

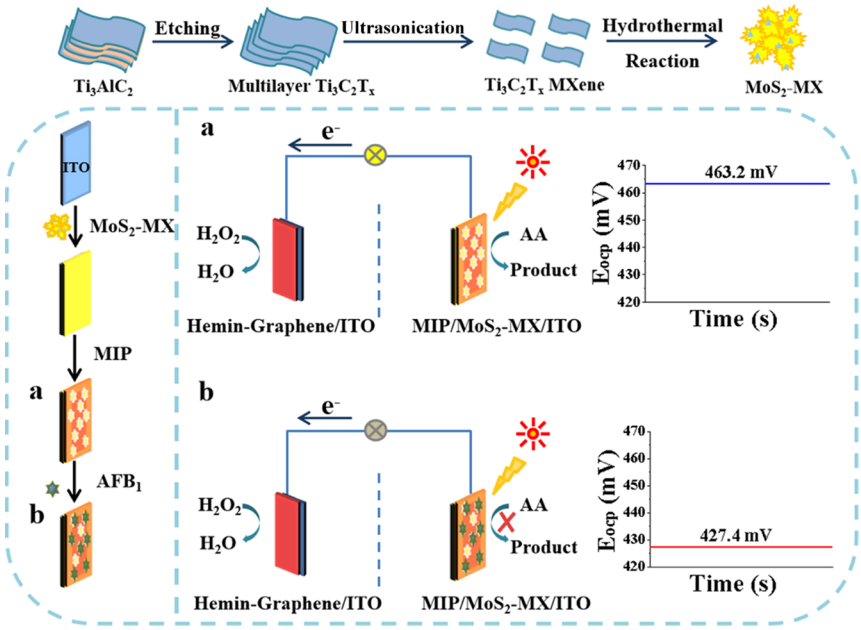

path to fabricate heterojunction photocatalysts to drive various redox reactions under appropriate light irradiation. Compared with the single semiconductor material, heterojunction can isolate electron−hole pairs to enhance electron transport.[15] Al-Ghamdi et al. discussed five types of heterojunctions in photocatalysts and explained the reason for their high photocatalytic activity.[16] The difference in conduction band (CB) and valence band (VB) levels or an additional electric field will accelerate the migrations of photogenerated electrons and holes to different semiconductors, resulting in a spatial separation of electron−hole pairs. Therefore, the introduction of MXene-based heterojunctions into PFC-assisted self-powered sensors may improve the photoelectric conversion efficiency.

Besides sensitivity, selectivity is also an important influential factor on the result of a sensor, especially in a complicated environment. Toxins such as AFB_1 are widely present in complex samples, such as rice, water, corn, and so on, with much interference.[17] The use of biorecognition elements is necessary, including proteins, antibodies, and oligonucleotides. In addition to such elements, molecular imprinting polymer (MIP) is a better alternative biorecognition element owing to its good selectivity, high chemical stability, flexible design, and low cost.[18] The specific recognition and capture capability of MIP depends on the size and shape of the generated cavities that perfectly match with the target molecules. So far, the MIP has been broadly applied in different analytical methods, including photoelectrochemistry, electrochemiluminescence, fluorescence, and electrochemical sensors. MIP-based sensors have been widely adopted in antibiotic,[19] protein,[20] and contaminant detection.[21] For example, Zhang et al. used graphitic carbon nitride ($g\text{-}C_3N_4$) and a MIP to realize sensitive detection of bisphenol A with a limitation of 1.3 μmol/L,[22] promoting the applicability of MIPs.

Herein, a novel self-powered biosensor was constructed by combining a PFC with MIP to achieve AFB_1 detection with high sensitivity and specificity. Considering that $Ti_3C_2T_x$ MXene was a good electron acceptor and had a protective effect on sulfide to some extent, $Ti_3C_2T_x$ MXene and MoS_2 were integrated to construct a heterojunction. The heterojunction exhibited better photoelectric response under light irradiation than $Ti_3C_2T_x$ MXene or MoS_2 alone, and the photogenerated holes of photoanodes could promote the oxidation of ascorbic acid (AA). The MoS_2−$Ti_3C_2T_x$ MXene heterojunction served as photoactive material and modified on an ITO surface to act as a photoanode. The MIP was formed on the surface of electrodes for specific recognition of AFB_1. Hemin-graphene (HG) modified electrodes were constructed as cathodes to catalyze the reduction of hydrogen peroxide. By combining the two electrodes together, a PFC could be developed to realize the self-powered detection of AFB_1. Only the target molecules could enter the MIP cavities and affect the open circuit potential (E_{ocp}) of the PFC, enabling the proposed self-powered sensor to realize specific and sensitive detection of AFB_1, as illustrated in Scheme 1.

EXPERIMENTAL SECTION

Materials and Apparatus. The detail is given in S1 in Supporting Information.

Synthesis of the MoS_2−MX Material. $Ti_3C_2T_x$ MXene was synthesized by etching Ti_3AlC_2 MAX phases and ultrasonic treatment, detailed experimental procedures are given in S3 in Supporting Information. The MoS_2−$Ti_3C_2T_x$ MXene heterojunction was prepared by a hydrothermal method. About 0.08 g of AMT and 0.18 g of $SC(NH_2)_2$ were added into 12 mL of $Ti_3C_2T_x$ MXene solution and stirred for 30 min. Then, the mixture solution was transferred to a Teflon reactor and reacted at 200 °C for 10 h. The products were collected by centrifugation and dried in a vacuum oven at 80 °C for 5 h.

Preparation of MIP/MoS_2−MX/ITO Electrodes. ITO electrodes were treated by ultrasonic washing with acetone, ethanol, and ultrapure water for 30 min and dried. Then, 100 μL of MoS_2−MX solution was added dropwise on the ITO electrode with a modified area of 1 cm^2 and dried at 60 °C for 2 h. Subsequently, the original solution that contained methacrylic acid (MAA), ethylene glycol dimethacrylate (EDMA), and azobisisobutyronitrile (AIBN) (molar ratios:

https://doi.org/10.1021/acs.analchem.1c02074
Anal. Chem. 2021, 93, 13204−13211

MAA/EDMA/AIBN = 8:3:1) and AFB_1 were mixed at a ratio of 2:1 and then added dropwise on the modified area of ITO. After ultraviolet-initiated polymerization for 10 min, the MIP/MoS_2−MX/ITO electrodes were obtained. As a control group, NIP/MoS_2−MX/ITO electrodes were prepared in the same way except adding AFB_1. The MIP/MoS_2−MX/ITO and the NIP/MoS_2−MX/ITO electrodes were eluted with ethanol for 20 min before use.

Preparation of HG/ITO Electrodes. First, 10 mg of graphene oxide (GO) powders were dispersed into 20 mL of water and treated with ultrasound for 2 h. The mixture was centrifuged at 3000 rpm for 5 min to remove a large chunk of GO, and then, GO solution was obtained. Then, 10 mg of hemin chloride powders were dissolved into 20 mL of water containing 0.2 mL ammonia hydroxide to get hemin solution. The above GO solution and hemin solution were mixed and transferred to a round-bottomed flask, and 30 μL of hydrazine hydrate solution was also added into the flask. After reaction at 65 °C for 3.5 h, the mixture was cooled down to room temperature and filtered through a nylon membrane with a pore diameter of 0.22 μm. The mixture was dissolved in water, and hemin-graphene solution (HG) was obtained. Finally, 100 μL of HG solution was added dropwise on the ITO electrode and dried to obtain HG/ITO electrodes.

Detection of AFB_1 with the Self-Powered Sensor. The MIP/MoS_2−MX/ITO electrodes were inserted into solutions of different concentrations of AFB_1 and reacted for 10 min to achieve specific capture of AFB_1. After being rinsed with ultrapure water, the electrodes were placed in 0.1 M PBS solution containing 0.03 M AA as photoanodes. At the same time, HG/ITO electrodes were placed in 0.1 M PBS solution containing 5 mM H_2O_2 as cathodes. Because of the difference of electrolytes, the photoanodes and cathodes were placed in a quartz cell separated by a Nafion membrane. During the experiment, the photoanodes were exposed to blue light at 465 nm and the cathodes were in a nitrogen atmosphere. The output signals of the PFC were recorded by collecting E_{ocp}−time curves to implement the detection.

RESULTS AND DISCUSSION

MoS_2−MX Enhanced Photoelectric Conversion Efficiency. Appropriate photoelectric materials were crucial for the photoelectric performance of the PFC. The hydrothermal method was applied to fabricate a new kind of MoS_2−MX heterojunction, which was first used as a photoanode modification material. SEM and TEM were used to characterize the morphology of the material. Figure 1A,B showed the SEM images of Ti_3AlC_2 and $Ti_3C_2T_x$ MXene, respectively. It was clear that Ti_3AlC_2 MAX phases were compact layered structures, while $Ti_3C_2T_x$ MXene phases owned fewer layers. After ultrasonic treatment, a thin-layer $Ti_3C_2T_x$ MXene structure could be obtained (Figure 1C). As illustrated in Figure S1A in Supporting Information and Figure 1D, pure MoS_2 powders were flower-like structures with a diameter of about 300 nm. On account of the rich functional groups of $Ti_3C_2T_x$ MXene, its surface tended to be negatively charged so that Mo^{6+} could be absorbed through static electricity to promote the growth of MoS_2 on the surface of $Ti_3C_2T_x$ MXene.[23] Obviously, MoS_2−MX powders displayed a similar structure as MoS_2 and $Ti_3C_2T_x$ MXene was evenly distributed (Figure 1E). To further prove the presence of $Ti_3C_2T_x$ MXene, high-resolution TEM (HRTEM) was performed. A clear lattice spacing of 0.62 nm corresponding to the (110) plane of the MoS_2 and 0.23 nm corresponding to the (103) plane of $Ti_3C_2T_x$ MXene appeared in Figure 1F.[24,25] In addition, the uniform distribution of Mo, Ti, and C also proved the successful synthesis of MoS_2−MX (Figure 1G−I). X-ray diffraction (XRD) patterns were used to characterize the crystal structure of the materials (Figure S1B in the Supporting Information). All results indicated the successful growth of MoS_2 in situ on the surface of $Ti_3C_2T_x$ MXene to form MoS_2−MX complexes.

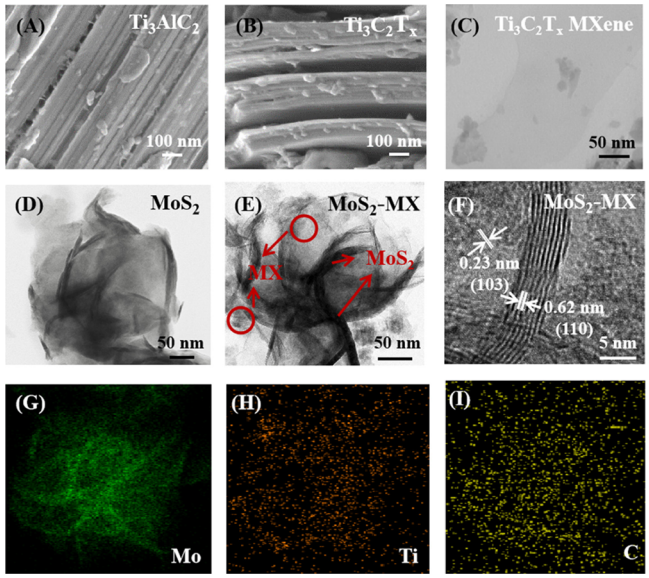

Figure 1. (A,B) SEM images of Ti_3AlC_2 and $Ti_3C_2T_x$ MXene, respectively. TEM images of $Ti_3C_2T_x$ MXene (C), MoS_2 (D), and MoS_2−MX (E), respectively. (F) HRTEM image of MoS_2−MX. (G−I) Corresponding element mapping of Mo, Ti, and C, respectively.

The chemical composition of MoS_2−MX was analyzed by X-ray photoelectron spectroscopy (XPS). It can be seen from Figure 2A that all elements including Mo, S, Ti, and C can be found in the energy spectrum. Three peaks could be clearly observed (Figure 2B), two of which belonged to the $3d_{3/2}$ peak (232.5 eV) and the $3d_{5/2}$ peak (229.3 eV) of Mo and the other peak belonged to the 2s peak (226.4 eV) of S. The results agreed with the reported research and showed that MoS_2 mainly contained trivalent Mo.[26] The binding energy of S 2p is also shown in Figure 2C. Furthermore, the ultraviolet−visible (UV−vis) adsorption spectrum was used to characterize the materials (Figure 2D). $Ti_3C_2T_x$ MXene showed no obvious absorption peak in the range of 200−400 nm, and MoS_2 showed strong absorption within the scope of 200−250 nm. As for MoS_2−MX, the absorption range was from 200 to 350 nm, which was wider than that for MoS_2. It might attribute to the fact that $Ti_3C_2T_x$ MXene can broaden the ultraviolet absorption of MoS_2, which was beneficial for realizing photoelectric conversion.

To solve the problem of low photoelectric conversion efficiency, MoS_2−MX was synthesized and modified on the ITO surface to act as a photoanode. By using MoS_2-modified and $Ti_3C_2T_x$ MXene-modified ITO as photoanodes, two control experiments were designed to testify the amplification effect of MoS_2−MX. As shown in Figure 2E, the photocurrent of MoS_2−MX was about 3-fold as much as that of MoS_2, while the photocurrent of $Ti_3C_2T_x$ MXene could be negligible. Furthermore, the E_{ocp} response under light irradiation of MoS_2−MX (490.8 mV) was obviously stronger than that of

https://doi.org/10.1021/acs.analchem.1c02074
Anal. Chem. 2021, 93, 13204−13211

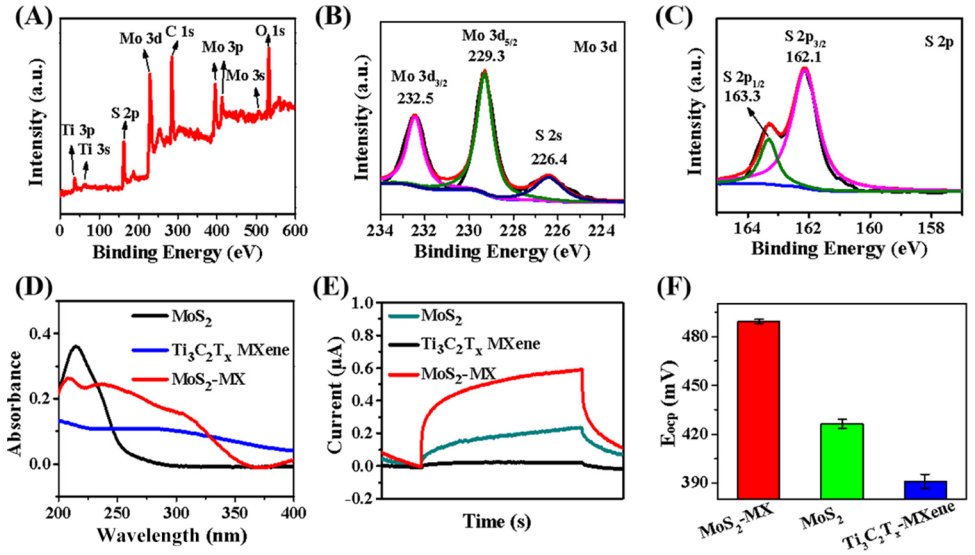

Figure 2. (A) XPS spectrum of MoS_2−MX. High-resolution XPS spectra of Mo 3d (B) and S 2p (C). (D) UV−vis adsorption spectrum of MoS_2, $Ti_3C_2T_x$ MXene, and MoS_2−MX. Photocurrent responses (E) and E_{ocp} (F) of the PFC constructed with different material-modified photoanodes in 0.1 M PBS containing 0.03 M AA.

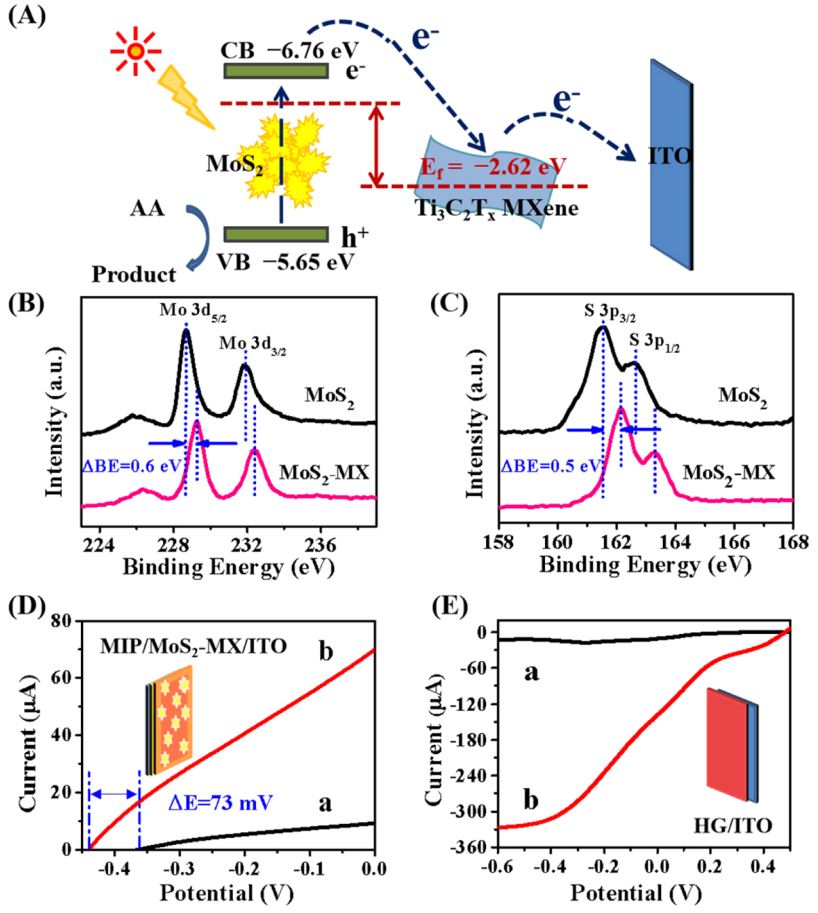

Figure 3. (A) Schematic diagram of the photocatalytic fuel cells. High-resolution XPS spectrum of Mo 3d (B) and S 2p (C) of MoS_2 and MoS_2−MX, respectively. (D) Polarization curves of the MIP/MoS_2−MX/ITO photoanode without (curve a) and with (curve b) light irradiation in 0.1 M PBS containing 0.03 M AA. (E) Polarization curves of the HG/ITO cathode without (curve a) and with (curve b) 5 mM H_2O_2 recorded in 0.1 M PBS at a scan rate of 2.0 mV/s.

MoS_2 (428.3 mV) or $Ti_3C_2T_x$ MXene (386.3 mV, Figure 2F). The reasons might be as follows: (1) as an excellent semiconductor material, MoS_2 can realize the conversion of light energy to electrochemical energy. (2) $Ti_3C_2T_x$ MXene was a good electron acceptor and could promote the electron−hole separation efficiency of MoS_2 to broaden the ultraviolet

https://doi.org/10.1021/acs.analchem.1c02074
Anal. Chem. 2021, 93, 13204−13211

absorption of MoS_2.[14] (3) $Ti_3C_2T_x$ MXene and MoS_2 formed heterojunction, which effectively inhibited the recombination of the photoelectrons and holes of MoS_2 to improve photoelectric conversion efficiency.

In general, MoS_2−MX was successfully synthesized and the application of MoS_2−MX as photoanode material enhanced the photocurrent by about threefold.

Experimental and Theoretical Exploration of the Developed Self-Powered Sensor. To explore the feasibility of the photocatalytic fuel cell constructed with MoS_2−MX and HG as the photoanode and cathode materials respectively, the energy band structure of the materials and transport behavior of the electrons were explored. The band diagrams of the CB and VB of MoS_2−MX were obtained based on the electron affinity (EA) and ionization potential (IP)[27] according to following formulas

$$\mathrm{IP} = -(4.80 - E_{1/2}^{\mathrm{Fc/Fc^+}} + E_{\mathrm{OX}}) \quad (1)$$

$$\mathrm{EA} = \mathrm{IP} + E_g \quad (2)$$

$$E_g = 1240/\lambda_{\mathrm{onset}} \quad (3)$$

where $E_{1/2}^{\mathrm{Fc/Fc^+}}$ was the formal potential of Fc/Fc^+, E_{ox} was the initial oxidation potential, E_g was the optical band gap, and λ_{onset} was first exciton absorption peak.[28,29]

The E_{ox} of MoS_2 can be obtained by cyclic voltammetry (CV), which was measured to be 2.36 V (Figure S2A in the Supporting Information). Similarly, $E_{1/2}^{\mathrm{Fc/Fc^+}}$ was characterized to be about 0.40 V (Figure S2A Inset in the Supporting Information). MoS_2 had an indirect band gap so that the Tauc plot graph of MoS_2 could be obtained by plotting the curve between $(\alpha h\nu)^{1/2}$ and $h\nu$, and then, a tangent line could be drawn to obtain E_g (the detailed process was shown in S4 in Supporting Information). It can be seen from Figure S2B in Supporting Information that the E_g was about 1.11 eV, which was in good agreement with the reported research.[30] According to the above data, the VB and CB of MoS_2 were calculated to be −5.65 and −6.76 eV respectively (the detailed calculation process is shown in S4 in Supporting Information). Theoretically, the Fermi level (E_f) of N-type semiconductors was slightly lower than its CB level. Therefore, the E_f of MoS_2 was about −6.76 eV. The E_f of $Ti_3C_2T_x$ MXene was reported to be about −2.62 eV,[31,32] which was much higher than that of MoS_2. Therefore, MoS_2 and $Ti_3C_2T_x$ MXene could form heterojunction, and electrons tended to migrate toward $Ti_3C_2T_x$ MXene, which could restrain electron−hole recombination and improve photoelectric conversion efficiency.

Furthermore, the binding energies of Mo and S of pure MoS_2 and the MoS_2−MX heterojunction were compared to explore the transport behaviors of electrons. As shown in Figure 3B,C, all the binding energies of MoS_2−MX shifted to a higher energy direction, displaying that it was more difficult for the MoS_2 in MoS_2−MX to lose electrons than pure MoS_2. The results also demonstrated that the electrons moved from MoS_2 to $Ti_3C_2T_x$ MXene and further to the surface of ITO, as illustrated in Figure 3A. Under light irradiation, MoS_2 could produce multiple photoelectrons and holes; the photogenerated holes could promote the oxidation of AA. Owing to the more positive E_f of $Ti_3C_2T_x$ MXene, photoelectrons tended to move to $Ti_3C_2T_x$ MXene and further to the ITO electrode to generate strong photocurrents.

For the self-powered sensor, if the initial potential of the anodic oxidation reaction was more negative than that of the cathodic reduction reaction, the PFC was thermodynamically feasible.[3] Using MIP/MoS_2−MX/ITO, Ag/AgCl, and Pt wire as the working, reference and counter electrode respectively, linear sweep voltammetry (LSV) in 0.1 M PBS containing 0.03 M AA with or without irradiation was performed. As shown in Figure 3D, the initial oxidation potentials of AA when the oxidation current was zero with and without irradiation were −437 and −364 mV (ΔE = 73 mV). Therefore, irradiation made the initial oxidation potential migrate to a more negative direction, which was beneficial to the oxidation of AA. During the experiment, irradiation intensity was found to have an impact on the initial oxidation potential of AA at the photoanode. ModuLight programmable lightsource (IVIUM Technologies BV, the Netherlands) was used to generate light, and irradiation intensity was adjusted by changing output voltages. As shown in Figure S3 in Supporting Information, 4 V was selected as optimum output voltage to produce enough irradiation intensity. Correspondingly, the reduction of H_2O_2 started at 400 mV and reached a plateau around −400 mV (Figure 3E). Therefore, MoS_2−MX-modified photoanodes could catalyze the oxidation reaction of AA under irradiation, and HG-modified cathodes realized the reduction of H_2O_2 under a higher potential, indicating the feasibility of building a fuel cell thermodynamically.

In short, the experimental data and theoretical calculation were discussed and analyzed to prove the feasibility of the construction of PFC-assisted self-powered sensors.

Feasibility and Reliability of the Self-Powered Sensor. In order to realize the specific detection of AFB_1, the MIP was used as a recognition element to construct a MIP/MoS_2−MX/ITO photoanode. The modification process of the photoanode was illustrated in Figure 4A. The MIP and

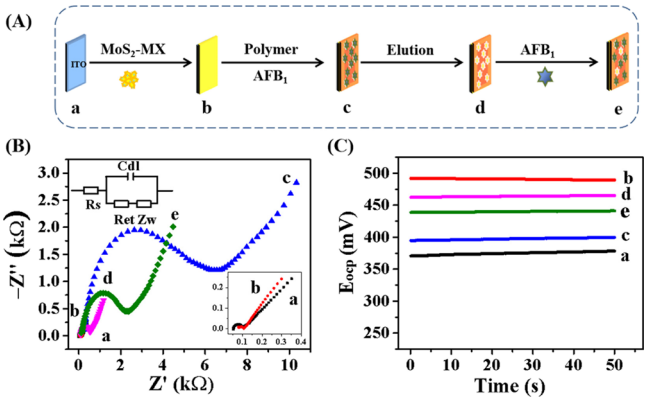

Figure 4. (A) Schematic diagram of the modification process of the photoanode. (B) EIS and (C) E_{ocp} of the PFC constructed with different material-modified photoanodes: (a) bare ITO, (b) MoS_2−MX/ITO, (c) MIP/MoS_2−MX/ITO without elution, (d) MIP/MoS_2−MX/ITO after elution, and (e) MIP/MoS_2−MX/ITO incubated with 10 ng/mL AFB_1.

MoS_2−MX served as biorecognition and photoelectric conversion element, respectively. Electrochemical impedance spectroscopy (EIS) was used to characterize the electron transport capability of different material-modified electrodes. As shown in Figure 4B, the resistance of the bare ITO electrode (curve a) was small. When MoS_2−MX was modified on the ITO electrode, the resistance decreased due to the good

https://doi.org/10.1021/acs.analchem.1c02074
Anal. Chem. 2021, 93, 13204−13211

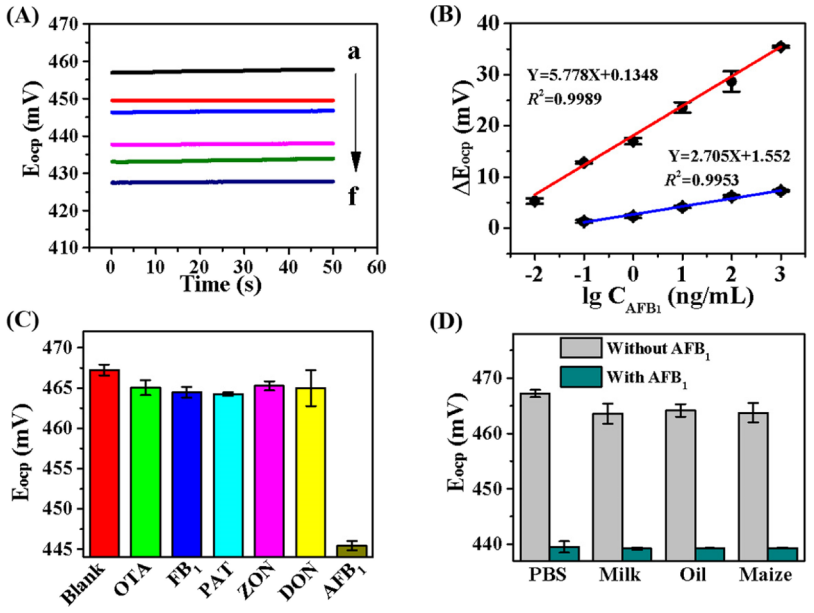

Figure 5. (A) E_{ocp} responses with different AFB_1 concentrations (0.01, 0.1, 1, 10, 100, and 1000 ng/mL). (B) Linear calibration curve between ΔE_{ocp} values and the logarithm of AFB_1 concentrations with (red line) and without light irradiation (blue line). (C) Selectivity of the proposed MIP−PEC sensor: 10 ng/mL of OTA, FB_1, PAT, ZON, and AFB_1 (1.0 ng/mL). (D) E_{ocp} responses of the self-powered biosensor in complex samples.

electrochemical conductivity of MoS_2−MX (curve b). The nonconductive MIP hindered the charge transfer on the electrode surface, resulting in a high resistance (curve c). The rapid decrease of resistance after elution indicated that the electron channels were formed, and the contact between the electrode and electron acceptor was provided (curve d). The presence of AFB_1 blocked the electron channel, and the resistance increased again (curve e). Similarly, E_{ocp} also showed the different responses of different material-modified photoanodes (Figure 4C). All results demonstrated the successful fabrication of the MIP/MoS_2−MX/ITO photoanode and the feasibility of the self-powered biosensor for specific recognition of AFB_1.

Likewise, the modification process and catalytic performance of HG/ITO electrodes were also investigated. It could be seen from Figure S4A in Supporting Information that HG/ITO had higher resistance than the ITO electrode, indicating that HG was successfully modified on the electrode. In order to investigate whether the cathode could catalyze the reduction of H_2O_2, the CV curves of the electrode were characterized. For the bare ITO electrode, only a very low cathode current was observed. When the electrode was modified by HG, a strong catalytic current can be observed because of the strong catalytic capacity of HG for the reduction of H_2O_2 (Figure S4B in Supporting Information).[33−35]

The ratio of $Ti_3C_2T_x$ MXene and MoS_2 as well as the concentration of MoS_2−MX were optimized to obtain higher response and detection sensitivity. The ratio of 1:5 and 1 mg/mL were chosen as optimal conditions (Figure S5A,B in Supporting Information). Furthermore, as an important factor in AFB_1 detection, the preparation conditions of the MIP also needed to be optimized to achieve optimal response. The elution time and incubation time were optimized. As seen in Figure S5C,D in Supporting Information, 20 and 10 min were selected as the elution and incubation time, respectively.

Analytical Performance of the Self-Powered Biosensor for AFB_1. Based on the integration of the MIP/MoS_2−MX/ITO photoanode with the HG/ITO cathode, a PFC-assisted self-powered biosensor was constructed for AFB_1 detection. To explore the influence of light irradiation, four control experiments with or without light irradiation in 0.1 M PBS with or without AFB_1 were designed. As shown in Figure S6 in Supporting Information, the sensor had the highest response in the presence of AFB_1 and light irradiation simultaneously. The E_{ocp} curves of the biosensor with different concentrations of AFB_1 were analyzed (Figure 5A). As shown in Figure 5B, the PFC-based SPES was more sensitive than the fuel cell (FC)-based SPES without irradiation by using AA and H_2O_2 as the anode and cathode electroactive molecules, respectively. Our PFC-based SPES can achieve sensitive detection of AFB_1 from 0.01 to 1000 ng/mL with a detection limit as low to 0.73 pg/mL. The self-powered biosensor exhibited a wider detection range and lower detection limit than the previously reported sensing methods for AFB_1 detection (Table S1 in Supporting Information).[36−41] It was worth nothing that the experimental slope was lower than the theoretical slope based on the Nernst equation ($59/n$), the possible reasons are shown in S8 in Supporting Information.

To characterize the stability of the self-powered sensor, the E_{ocp} values of eight photoanodes after reaction with 10 ng/mL AFB_1 were measured. There was nearly no difference between the eight electrodes, showing the good stability of the sensor (Figure S7A in Supporting Information). Furthermore, when the E_{ocp} of the PFC was measured under continuous illumination for 400 s, it could be seen that there was still no change (Figure S7B in Supporting Information). In order to characterize the storage stability of MIP/MoS_2−MX/ITO photoanodes and HG/ITO cathodes, the E_{ocp} values were continuously collected for 7 days. Both photoanodes and cathodes were stored at 4 °C before the test. From Figure S7C in Supporting Information, it can be seen that the PFC could keep at least 97% of the initial response, revealing the high stability of the modified electrodes. Selectivity was very important for sensors to ensure the reliability of the results.

https://doi.org/10.1021/acs.analchem.1c02074
Anal. Chem. 2021, 93, 13204−13211

Five other toxins were used as control samples. As shown in Figure 5C, only the presence of AFB_1 can cause obvious decrease of E_{ocp}, while the change of control samples can be negligible, demonstrating good specificity, as well as prospect for application in complex samples.

Toxins are widely present in the complex samples of rice, corn, water, and so on, which have much interference. AFB_1 (10 ng/mL) was added to milk, groundnut oil, and maize to obtain positive samples. Negative samples were obtained with the same operation without adding AFB_1. As seen in Figure 5D, all positive samples caused an obvious decrease in the E_{ocp} that was similar to the result in the buffer of PBS. In contrast, the negative samples without AFB_1 could not be specifically captured by the MIP on the photoanode surface, thus causing a change in E_{ocp}. As shown in Table S2, the recovery rate of the self-powered sensor in complex samples was determined to be 92.0−104.2%, indicating excellent selectivity and anti-interference ability of the sensor.

CONCLUSIONS

In summary, a self-powered biosensor by combining photocatalytic fuel cells with molecularly imprinted membranes was constructed to achieve sensitive and specific detection of AFB_1. PFCs rather than other fuel cells were used as signal conversion elements, achieving high output signals and good stability. MoS_2−MX served as the photoanode material for the first time, and the heterojunction structure enhanced the photocurrent under light irradiation by about 3-fold. MIPs solved the limited selectivity and achieved the low-abundant detection of AFB_1 with a detection limit of 0.73 pg/mL. On account of the above properties, the proposed self-powered biosensor can reach good specificity and accuracy in complex environments, which indicated its potential application in food safety and environmental monitoring.

ASSOCIATED CONTENT

Supporting Information

The Supporting Information is available free of charge at https://pubs.acs.org/doi/10.1021/acs.analchem.1c02074.

SEM image of MoS_2 and XRD patterns valence band and conduction band analysis of MoS_2, optimal experiments of irradiation intensity, characterization of the HG electrode, optimal experiments of the ratio of composition, concentration of MoS_2−MX, elution time and incubation time, ΔE_{ocp} responses of the self-powered biosensor under different conditions, reproducibility and stability study of self-powered biosensor, comparison of this method with some other reported methods for the AFB_1 assay, and comparison of this method with some other reported methods for the AFB_1 assay (PDF)

AUTHOR INFORMATION

Corresponding Authors

Zhen Wu − *Hubei Collaborative Innovation Center for Advanced Organic Chemical Materials, Ministry of Education Key Laboratory for the Synthesis and Application of Organic Functional Molecules & College of Chemistry and Chemical Engineering, Hubei University, Wuhan 430062, PR China*; Email: wuzhen@hubu.edu.cn

Shengfu Wang − *Hubei Collaborative Innovation Center for Advanced Organic Chemical Materials, Ministry of Education Key Laboratory for the Synthesis and Application of Organic Functional Molecules & College of Chemistry and Chemical Engineering, Hubei University, Wuhan 430062, PR China*; orcid.org/0000-0001-7175-4908; Phone: 0086-27-50865309; Email: wangsf@hubu.edu.cn; Fax: 0086-27-88663043

Authors

Yunxia Jin − *Hubei Collaborative Innovation Center for Advanced Organic Chemical Materials, Ministry of Education Key Laboratory for the Synthesis and Application of Organic Functional Molecules & College of Chemistry and Chemical Engineering, Hubei University, Wuhan 430062, PR China*

Yang Luan − *Hubei Collaborative Innovation Center for Advanced Organic Chemical Materials, Ministry of Education Key Laboratory for the Synthesis and Application of Organic Functional Molecules & College of Chemistry and Chemical Engineering, Hubei University, Wuhan 430062, PR China*

Wei Wen − *Hubei Collaborative Innovation Center for Advanced Organic Chemical Materials, Ministry of Education Key Laboratory for the Synthesis and Application of Organic Functional Molecules & College of Chemistry and Chemical Engineering, Hubei University, Wuhan 430062, PR China*; orcid.org/0000-0001-6138-7470

Xiuhua Zhang − *Hubei Collaborative Innovation Center for Advanced Organic Chemical Materials, Ministry of Education Key Laboratory for the Synthesis and Application of Organic Functional Molecules & College of Chemistry and Chemical Engineering, Hubei University, Wuhan 430062, PR China*; orcid.org/0000-0003-3586-9921

Complete contact information is available at: https://pubs.acs.org/10.1021/acs.analchem.1c02074

Notes

The authors declare no competing financial interest.

ACKNOWLEDGMENTS

Financial support by the National Natural Science Foundation of China (21904032, 21775033, and 22076041).

REFERENCES

(1) Katz, E.; Bückmann, A. F.; Willner, I. *J. Am. Chem. Soc.* **2001**, *123*, 10752−10753.
(2) Wang, B.; Liu, Y.; Zhou, Y.; Wen, Z. *Nano Energy* **2018**, *46*, 322−330.
(3) Yan, K.; Yang, Y.; Okoth, O. K.; Cheng, L.; Zhang, J. *Anal. Chem.* **2016**, *88*, 6140−6144.
(4) Yang, H.; Zhou, M.; Liu, M.; Yang, W.; Gu, T. *Biotechnol. Lett.* **2015**, *37*, 2357−2364.
(5) Ivars-Barceló, F.; Zuliani, A.; Fallah, M.; Mashkour, M.; Rahimnejad, M.; Luque, R. *Appl. Sci.* **2018**, *8*, 1184.
(6) Fu, L.; Liu, J.; Hu, Z.; Zhou, M. *Electroanalysis* **2018**, *30*, 2535−2550.
(7) Zhou, M. *Electroanalysis* **2015**, *27*, 1786−1810.
(8) Chen, Y.; Ji, W.; Yan, K.; Gao, J.; Zhang, J. *Nano Energy* **2019**, *61*, 173−193.
(9) Gai, P.; Gu, C.; Hou, T.; Li, F. *Anal. Chem.* **2017**, *89*, 2163−2169.
(10) Yan, K.; Zhu, Y.; Ji, W.; Chen, F.; Zhang, J. *Anal. Chem.* **2018**, *90*, 9662−9666.
(11) Yan, K.; Ji, W.; Zhu, Y.; Chen, F.; Zhang, J. *Chem. Commun.* **2019**, *55*, 12040−12043.

(12) Naguib, M.; Kurtoglu, M.; Presser, V.; Lu, J.; Niu, J.; Heon, M.; Hultman, L.; Gogotsi, Y.; Barsoum, M. W. *Adv. Mater.* **2011**, *23*, 4248−4253.
(13) Xie, X.; Zhang, N. *Adv. Funct. Mater.* **2020**, *30*, 2002528.
(14) Wang, H.; Wu, Y.; Yuan, X.; Zeng, G.; Zhou, J.; Wang, X.; Chew, J. W. *Adv. Mater.* **2018**, *30*, 1704561.
(15) Xu, H.; Ren, A.; Wu, J.; Wang, Z. *Adv. Funct. Mater.* **2020**, *30*, 2000907.
(16) Low, J.; Yu, J.; Jaroniec, M.; Wageh, S.; Al-Ghamdi, A. A. *Adv. Mater.* **2017**, *29*, 1601694.
(17) Gao, J.; Yao, X.; Chen, Y.; Gao, Z.; Zhang, J. *Anal. Chem.* **2021**, *93*, 677−682.
(18) Mao, L.; Ji, K.; Yao, L.; Xue, X.; Wen, W.; Zhang, X.; Wang, S. *Biosens. Bioelectron.* **2019**, *127*, 57−63.
(19) Luo, Q.; Yu, N.; Shi, C.; Wang, X.; Wu, J. *Talanta* **2016**, *161*, 797−803.
(20) Ma, X.-T.; He, X.-W.; Li, W.-Y.; Zhang, Y.-K. *Sens. Actuators, B* **2017**, *246*, 879−886.
(21) Villa, C. C.; Sánchez, L. T.; Valencia, G. A.; Ahmed, S.; Gutiérrez, T. J. *Trends Food Sci. Technol.* **2021**, *111*, 642−669.
(22) Yan, K.; Yang, Y.; Zhang, J. *Sens. Actuators, B* **2018**, *259*, 394−401.
(23) Jiao, S.; Liu, L. *Ind. Eng. Chem. Res.* **2019**, *58*, 18141−18148.
(24) Alomar, M.; Liu, Y.; Chen, W.; Fida, H. *Appl. Surf. Sci.* **2019**, *480*, 1078−1088.
(25) Jiang, Q.; Wang, H.; Wei, X.; Wu, Y.; Gu, W.; Hu, L.; Zhu, C. *Anal. Chim. Acta* **2020**, *1119*, 11−17.
(26) Wu, X.; Wang, Z.; Yu, M.; Xiu, L.; Qiu, J. *Adv. Mater.* **2017**, *29*, 1607017.
(27) Dissanayake, D. M. N. M.; Lutz, T.; Curry, R. J.; Silva, S. R. P. *Appl. Phys. Lett.* **2008**, *93*, 043501.
(28) Li, S.; Yuan, Z.; Deng, P.; Sun, B.; Zhang, Q. *Polym. Chem.* **2014**, *5*, 2561−2566.
(29) Hou, J.; Tan, Z. A.; Yan, Y.; He, Y.; Yang, C.; Li, Y. *J. Am. Chem. Soc.* **2006**, *128*, 4911−4916.
(30) Liu, X.; Huo, X.; Liu, P.; Tang, Y.; Xu, J.; Liu, X.; Zhou, Y. *Electrochim. Acta* **2017**, *242*, 327−336.
(31) Pi, Y.; Li, Z.; Xu, D.; Liu, J.; Li, Y.; Zhang, F.; Zhang, G.; Peng, W.; Fan, X. *ACS Sustainable Chem. Eng.* **2017**, *5*, 5175−5182.
(32) Ran, J.; Gao, G.; Li, F.-T.; Ma, T.-Y.; Du, A.; Qiao, S.-Z. *Nat. Commun.* **2017**, *8*, 13907.
(33) Lin, Y.; Wu, L.; Huang, Y.; Ren, J.; Qu, X. *Chem. Sci.* **2015**, *6*, 1272−1276.
(34) Guo, Y.; Deng, L.; Li, J.; Guo, S.; Wang, E.; Dong, S. *ACS Nano* **2011**, *5*, 1282−1290.
(35) Guo, Y.; Li, J.; Dong, S. *Sens. Actuators, B* **2011**, *160*, 295−300.
(36) Bhardwaj, H.; Pandey, M. K.; Rajesh, S. G.; Sumana, G. *Microchim. Acta* **2019**, *186*, 592.
(37) Sun, C.; Liao, X.; Jia, B.; Shi, L.; Zhang, D.; Wang, R.; Zhou, L.; Kong, W. *Microchim. Acta* **2020**, *187*, 236.
(38) Wang, B.; Chen, Y.; Wu, Y.; Weng, B.; Liu, Y.; Lu, Z.; Li, C. M.; Yu, C. *Biosens. Bioelectron.* **2016**, *78*, 23−30.
(39) Pan, D.; Li, G.; Hu, H.; Xue, H.; Zhang, M.; Zhu, M.; Gong, X.; Zhang, Y.; Wan, Y.; Shen, Y. *Chem.—Eur J.* **2018**, *24*, 9869−9876.
(40) Yagati, A. K.; Chavan, S. G.; Baek, C.; Lee, M.-H.; Min, J. *Sensors* **2018**, *18*, 1320.
(41) Liu, X.; Fan, D.; Duan, S.; Bao, C.; Wang, H.; Wang, X.; Sun, X.; Wei, Q. *Anal. Methods* **2019**, *11*, 3890−3897.

https://doi.org/10.1021/acs.analchem.1c02074
Anal. Chem. 2021, 93, 13204−13211